Probabilistic forecast using a Lagrangian sea ice model: application for search and rescue operations

Matthias Rabatel[1], Pierre Rampal[1], Alberto Carrassi[1], Laurent Bertino[1], and Christopher K. R. T. Jones[2]

[1]Nansen Environmental and Remote Sensing Center, Norway
[2]Department of Mathematics, University of North Carolina, USA

Correspondence to: Rabatel (matthias.rabatel@nersc.no or matthiasrabatel@gmail.com)

Abstract. We present a sensitivity analysis, and discuss the probabilistic forecast capabilities, of the novel sea ice model *neXtSIM*. The study pertains to the response of the model to the uncertainty on winds using probabilistic forecasts of ice trajectories. *neXtSIM* is a continuous Lagrangian numerical model, and uses an elasto-brittle rheology to simulate the ice response to external forces. The sensitivity analysis is based on a Monte Carlo sampling of 12 members. The response of the
5   model to the uncertainties is evaluated in terms of simulated ice drift distances from their initial positions, and from the mean position of the ensemble, over the mid-term forecast horizon of 10-days. The simulated ice drift is decomposed into advective and diffusive parts that are characterised separately both spatially and temporally and compared to what is obtained with a *free-drift* model, that is, when the ice rheology does not play any role on the modelled physics of the ice. The seasonal variability of the model sensitivity is presented, and shows the role of the ice compactness and rheology in the ice drift response at both local
10 and regional scales in Arctic. Indeed, the ice drift simulated by *neXtSIM* in summer is close to the one obtained with the free-drift model, while the more compact and solid ice pack shows a significantly different mechanical and drift behaviour in winter. For the winter period analysed in this study, we also show that, in contrast to of free-drift model, *neXtSIM* reproduces the sea ice Lagrangian diffusion regimes as found from observed trajectories. The forecast capability of *neXtSIM* is also evaluated using a large set of real buoys' trajectories, and compared to the capability of the free-drift model. We found that *neXtSIM*
15 performs significantly better in simulating sea ice drift, both in terms of forecast error and as a tool to assist search-and-rescue operations, although the sources of uncertainties assumed for the present experiment are not sufficient for a complete coverage of the observed IABP positions.

1   Introduction

Large changes in the Arctic sea ice have been observed in recent decades in terms of the ice thickness, extent and drift (e.g.
20 Kwok, 2007; Stroeve et al., 2007; Rampal et al., 2011; Stroeve et al., 2012). These changes, and the underlying driving mechanisms, still need to be fully understood in spite of their being fundamental for building confidence in the forecasting capabilities of current prediction systems. The need for a reliable sea ice prediction platform is particularly felt in the modern context of growing economic opportunities with high societal and environmental impacts. For instance, the dramatic decline of sea ice cover in the Arctic is opening new shipping routes, fishing grounds and tourist destinations as well as access to a significant

portion of the remaining hydrocarbon resources. Associated with this increasing activity are important risks for pollution of the Arctic environment, and risk to human lives. High quality predictions of ocean and sea ice in the polar regions are therefore needed in order to measure the risks, to plan future activities, and to assist operations in real time.

5   Current short-term (i.e. within 10 days) forecasting systems integrate either a stand-alone sea ice model (RIPS (Lemieux et al., 2016)), a coupled ice-ocean model (such as, e.g. ACNFS (Hebert et al., 2015), TOPAZ (Sakov et al., 2012) or GIOPS (Smith et al., 2015)), or more seldom a coupled atmosphere-ice-ocean model (GloSea5 (Williams et al., 2015)). Seasonal to decadal climate forecasts are more common and include sea ice as part of the Earth System Models (see, e.g. Carrassi et al. (2016)). The sea ice models used in these systems are usually derived from the work of Hibler III (1979), and they treat the
10   sea ice as a continuous medium with a viscous-plastic rheology (Hunke and Dukowicz, 1997; Bouillon et al., 2009). In spite of this development, simple free-drift ice (i.e. in the absence of friction and internal forces) forecasts have remained in use by environment agencies (Grumbine, 1998, 2003). The forecast skill of these systems based on a free-drift ice has been evaluated in deterministic mode, when a single "best" forecast is provided: despite the lack of realism in the free-drift assumption, the forecast skill of such systems is seen as difficult to beat (Schweiger and Zhang, 2015).

15

Probabilistic forecasts, widely used in weather forecasting (Molteni et al., 1996; Leutbecher and Palmer, 2008), are still in their infancy in sea ice forecasting. Probabilistic predictions rely on an ensemble of model simulations (i.e. a Monte Carlo simulation) used to describe the forecast uncertainty stemming from errors in the model parameters, initial and boundary conditions as well as from any external forcing. The resulting cloud of model outputs is used to retrieve statistical information,
20   such as the ensemble mean and its spread (i.e. the standard deviation), that are thus used in place of the deterministic forecast and to estimate the associated uncertainty, respectively. The multiple simultaneous sources of errors make the forecast accuracy of the ensemble mean usually exceed that of the single deterministic prediction (Leith, 1974; Zhu, 2005), although often the spread underestimates the actual forecast error when the sources of error are not all adequately accounted for (Buizza et al., 2005). Monte Carlo techniques are already common practice in different areas (e.g. Dobney et al., 2000; Hackett et al., 2006;
25   Breivik and Allen, 2008; Melsom et al., 2012; Motra et al., 2016; Duraisamy and Iaccarino, 2017), and a common tool for sensitivity analysis.

This study concerns the probabilistic forecast capability of the sea ice model *neXtSIM* (Rampal et al., 2016b). The work is carried out by performing a Monte Carlo sensitivity analysis of the model with respect to uncertainties in the surface wind velocity. The first goal is to highlight the role of the ice rheology on the ice drift: how do the ensemble mean drift and its
30   standard deviation respond to uncertainties in the wind forcing? To answer this question, we compare the ice drift obtained from *neXtSIM* to one obtained from a *free-drift* model. In the second part, we study the skill of the probabilistic forecast using Lagrangian trajectories departing from independent in situ drifting buoys, and compare them with real observations. Without aiming to make it a key objective. We use the conceptual framework of search and rescue operations where a probabilistic
35   forecast is commonly used to draw the search area of the ocean where drifting objects are likely to be found (Hackett et al.,

2006; Breivik and Allen, 2008; Melsom et al., 2012).

Our main research tool and object of study is the advanced sea ice model *neXtSIM*. The model *neXtSIM* is based on a Lagrangian numerical scheme and on a continuous approach using a newly developed elasto-brittle ice rheology. This mechanical framework is inspired by the scaling properties of sea ice dynamics revealed by multi-scale statistical analyses of observed sea ice drift and deformation (Marsan et al. (2004), Rampal et al. (2008) and Bouillon and Rampal (2015b)), as well as by the in situ measures of sea ice internal stresses showing that sea ice deformation is accommodated by Coulombic faulting (Weiss et al. (2007), Weiss and Schulson (2009)). For 40 years, a large variety of sea ice models have been developed. Some, like *neXtSIM*, treat the sea ice as a continuous medium, yet with different rheologies (e.g. visco-plastic (Coon et al., 1974; Hibler III, 1979), elasto-visco-plastic, (Hunke and Dukowicz, 1997), or Maxwell-elasto-brittle, (Dansereau, 2016)), are suitable for high ice concentration ($> 80\%$) while others, that treat the ice as a discrete medium (Hopkins et al., 2004; Wilchinsky et al., 2010; Herman, 2011; Rabatel et al., 2015), are more suitable for low ice concentration ($< 80\%$) such as within the marginal ice zone.

We concentrate here on the impact of the error from the wind field alone. The reasons are twofold: first, the wind is the most influential external force affecting sea ice motion. About 70% of the variance of the sea ice motion in the central Arctic can be explained by the geostrophic winds (Thorndike and Colony, 1982). However, the sea ice response to winds strongly depends on its degree of damage; sea ice responds in a linear way only when it is fragmented into small floes, whereas this behaviour drastically changes when considering a large, continuous and undamaged solid plate. The second reason stands on the fact that surface wind velocity fields provided by atmospheric re-analyses contain large uncertainties in the Arctic.

Previous sensitivity analyses of the *neXtSIM* model have been performed with respect to initial conditions and to some key sea ice mechanical parameters (see Sect. 4 in Bouillon and Rampal (2015a)). These analyses consisted in running the model with different values of the input sources. This allowed the authors to explore and quantify the sensitivity of the ice velocity with respect to the ratio between water and air drag coefficients, and of the ice deformation with respect to the compactness parameter value (see Eq. (5)), the sea ice cohesion value (see Eq. (10) in Bouillon and Rampal (2015a)), the initial concentration field, or the initial thickness field. Although these analyses did not use the full complexity of the present version of *neXtSIM* (in particular they did not include the thermodynamics, nor the re-meshing process), the impact of some mechanical parameters on the ice deformation can still be considered as valid.

This paper is organized as follow: Sect. 2 gives a general presentation of the sea ice model *neXtSIM* with the main equations describing the sea ice dynamical behaviour; Sect. 3 presents the details of the sensitivity analysis based on a Monte Carlo sampling, including the description of the quantities of interest, the construction of the wind perturbations, and the general experimental setup. In the same Sect. 3, we also define the *free-drift* model that will be used for comparison and benchmark

against *neXtSIM*. Section 4 discusses the results for the ensemble mean, spread and the evaluation of the forecast skills comparing *neXtSIM* to the *free-drift* model. Final conclusion are drawn in Sect. 5.

2 Generalities on the model *neXtSIM*

In this section, we provide a general description *neXtSIM*. Deliberately, we choose to not go through all model equations here,
but rather list those that are needed to get an overall understanding of how the model works, and that are relevant for the present
study. For a more detailed description of the model see Bouillon and Rampal (2015a) and Rampal et al. (2016b).

neXtSIM is a continuous dynamic-thermodynamic sea ice model. It uses a pure Lagrangian advection scheme, meaning that
the nodes of the model mesh are moving at each time step according to the simulated ice motion. The model mesh is therefore
changing over time, it is not spatial homogeneous, and it can locally become highly distorted, that is, when and where the
ice motion field is showing strong spatial gradients. In this case, a local and conservative re-meshing procedure is applied in
order to keep the numerical integrity of the model and the spatial resolution of the grid approximatively constant during the
simulation. The equations are discretised on a triangular mesh and solved using the classical finite element method, with scalar
and tensorial variables defined at the center of the mesh elements, and vectors defined at the vertices. The model is using a
mechanical framework that has been developed recently (Girard et al. (2009) and Bouillon and Rampal (2015a)), and which is
based on the Elasto-Brittle (EB) rheology. The brittle mechanical behaviour of the sea ice is simulated by calculating the local
level of damage in each grid cell, a variable which is not considered in classical viscous-plastic sea ice models typically used
in the sea ice modelling community. Sea ice thermodynamic, which is parametrised in *neXtSIM* as in the zero-layer model
of Semtner (1976), controls the amount of ice formed or melted at each time step. When a volume of new (and therefore
undamaged) ice is formed within a grid cell by thermodynamical refreezing, the mechanical strength of the total volume of ice
covering that cell is partially restored, and the new damage value is computed as a volume-weighted mean. Note however that
the damaging process is very fast (i.e. about few minutes) while the mechanical healing process is occurring over much slower
time scales of about several weeks. The sea ice variables used in *neXtSIM* are the following: h and h_{s} are the effective sea ice
and snow thickness respectively; A is the sea ice concentration; d is the sea ice damage ranging from 0 (undamaged ice) to
1 (fully damaged); $\boldsymbol{u}$ is the horizontal sea ice velocity vector; and $\boldsymbol{\sigma}$ is the ice internal stress tensor. The model has two ice
thickness categories: ice and open water.

The evolution equations for h, h_{s} and A (here denoted ϕ) have the following generic form

$$\frac{D\phi}{Dt} = -\phi \nabla \cdot \boldsymbol{u} + S_{\phi},\tag{1}$$

where $\frac{D\phi}{Dt}$ is the material derivative of ϕ, $\nabla \cdot \boldsymbol{u}$ the divergence of the horizontal velocity and S_{ϕ} a thermodynamical sink/source
term. The evolution of sea ice velocity comes from the following sea ice momentum equation, integrated over the vertical,

$$m\frac{D\boldsymbol{u}}{Dt} = \nabla \cdot (\boldsymbol{\sigma}h) - \nabla P + \boldsymbol{\tau}_{\mathrm{a}} + \boldsymbol{\tau}_{\mathrm{w}} + \boldsymbol{\tau}_{\mathrm{b}} - mf\boldsymbol{k} \wedge \boldsymbol{u} - m\boldsymbol{g}\nabla\eta,\tag{2}$$

where m is the inertial mass, P is a pressure term, $\boldsymbol{\tau}_\mathrm{a}$ is the surface wind (air) stress, $\boldsymbol{\tau}_\mathrm{w}$ is the ocean (water) stress and $\boldsymbol{\tau}_\mathrm{b}$ is the basal stress in case of grounded ice parametrised as in Lemieux et al. (2015). The last terms are the Coriolis parameter, f, the upward pointing unit vector, $\boldsymbol{k}$, the gravity acceleration, $\boldsymbol{g}$, and the ocean surface elevation, η. The internal stress $\boldsymbol{\sigma}$ is computed as in Bouillon and Rampal (2015a) and Rampal et al. (2016b). Its evolution equation can be written as

$$\frac{D\boldsymbol{\sigma}}{Dt} = \frac{\Delta d}{Dt}\frac{\partial \boldsymbol{C}}{\partial d} : \boldsymbol{\epsilon} + \boldsymbol{C}(A,d) : \dot{\boldsymbol{\epsilon}}, \tag{3}$$

where d is the damage and $\dot{\boldsymbol{\epsilon}}$ is the deformation rate tensor defined as $\dot{\boldsymbol{\epsilon}} = \frac{1}{2}\left(\nabla\boldsymbol{u} + (\nabla\boldsymbol{u})^\mathrm{T}\right)$. $\boldsymbol{C}$ can be written as

$$\boldsymbol{C} = \frac{E(A,d)}{(1-\nu^2)}\begin{bmatrix} 1 & \nu & 0 \\ \nu & 1 & 0 \\ 0 & 0 & \frac{1-\nu}{2} \end{bmatrix} \tag{4}$$

with ν being the Poisson's ratio while $E(A,d)$ the effective elastic stiffness of the ice which depends on the ice concentration A and the damage d according to

$$E = Ye^{-\alpha(1-A)}(1-d) \tag{5}$$

where Y is the sea ice elastic modulus (Young's modulus) and α is the so-called compactness parameter.

The evolution equation for the damage is written as:

$$\frac{Dd}{Dt} = \frac{\Delta d}{\Delta t} + S_d, \tag{6}$$

where Δd is a damage source term calculated as in Rampal et al. (2016b) (Eq. (8)), and S_d is thermodynamical sink term which depends on the volume of new and undamaged ice formed over one time step as well as on time (See Rampal et al. (2016b), Sect. 2.3 for more details).

The air and oceanic drags, respectively $\boldsymbol{\tau}_\mathrm{a}$ and $\boldsymbol{\tau}_\mathrm{w}$ in Eq. (2), are written as a force per unit area in the quadratic form using the associated turning angle (Leppäranta, 2011)

$$\begin{aligned} \boldsymbol{\tau}_\mathrm{a} &= \rho_a C_a \|\boldsymbol{u}_\mathrm{a} - \boldsymbol{u}\| R_{\theta_a}(\boldsymbol{u}_\mathrm{a} - \boldsymbol{u}) \\ \boldsymbol{\tau}_\mathrm{w} &= \rho_w C_w \|\boldsymbol{u}_\mathrm{w} - \boldsymbol{u}\| R_{\theta_w}(\boldsymbol{u}_\mathrm{w} - \boldsymbol{u}) \end{aligned} \tag{7}$$

where $\|.\|$, R_{θ_a}, R_{θ_w}, $\boldsymbol{u}_\mathrm{a}$, $\boldsymbol{u}_\mathrm{w}$, ρ_a, ρ_w, C_a and C_w are, respectively, the Euclidean norm in $\mathbb{R}^2$, the rotation matrix through the angle θ_a and θ_w, the wind velocity, the ocean current, the air density, the water density, the air drag coefficient and the water drag coefficient.

3 Sensitivity analysis

The sensitivity, or uncertainty analysis, are performed in order to understand and to quantify the relative importance of different input sources in the outputs. More specifically, we explore the output space of the model and, after the definition of a region of interest for this output space, we identify which model inputs and which values and uncertainties of the inputs better explain the model results in the chosen region. This type of analysis is an usual important previous step to determine optimal sampling strategies for both probabilistic forecast and ensemble-based data assimilation methods (e.g. Evensen, 2009).

The Cryosphere
Discussions

3.1 Methodology

In this study, we perform a sensitivity analysis using a statistical approach based on Monte Carlo sampling of the model inputs. We focus on the response of the model to the uncertainties in the wind velocity field. In particular, we are looking at the response of sea ice drift to wind perturbations representing these uncertainties. Our methodology is based on simulating Lagrangian trajectories of virtual buoys using an ensemble run of the *neXtSIM* model forced by slightly different (i.e. perturbed) wind forcing (see Sect. 3.2 for more details on the generation of the perturbed winds).

The velocity of a given buoy is calculated on-line, at each time step, as a linear interpolation of the velocities simulated at the nodes of the mesh element containing that buoy (see Lagrangian approach in Sect. 2). Each virtual buoy is associated with a initial position $x_0 \in D$, with D being the initial domain, and a start date $t_0 \in Y$ where Y is the time period of interest of this study (see Sect. 3.2 for more details). A buoy trajectory is denoted $\boldsymbol{g}(x_0, t_0, t)$ with $t \in [t_0, T]$, and where T defines the duration of the individual simulations. For each initial position x_0 and start date t_0, we simulate N trajectories $\{\boldsymbol{g}_i\}_{i \in \{1,\ldots,N\}}$ from N model runs, each one corresponding to a different realisation of the wind forcing. If a buoy ends up in an ice-free element, it is then untracked further and its trajectory discarded from the remaining analysis.

For each ensemble member (trajectory), we define the following Euclidean distances

$$\forall i \in \{1, \ldots, N\},$$
$$
\begin{aligned}
r_i(t) &= \|\boldsymbol{g}_i(\boldsymbol{x}_0, t_0, t) - \boldsymbol{x}_0\| \\
b_i(t) &= \|\boldsymbol{g}_i(\boldsymbol{x}_0, t_0, t) - \boldsymbol{B}(t)\|,
\end{aligned}
$$

where the quantity $r_i(t)$ is the distance of the member position at time t, $\boldsymbol{g}_i(\boldsymbol{x}_0, t_0, t)$, from its departure origin, $\boldsymbol{x}_0 = \boldsymbol{g}_i(t = t_0)$. The second quantity, $b_i(t)$, represents the distance between the member position at time t and the ensemble mean position (i.e. the barycentre, $\boldsymbol{B}(t)$, of the ensemble), $\boldsymbol{B}(t) = \sum_{i=1}^{N} \boldsymbol{g}_i(\boldsymbol{x}_0, t_0, t)$, at the same time t (see the top panel of Fig. 1). We make use here of the convention of using boldface for vectors and matrices and normal face for scalar quantities; hereafter, we drop the explicit mention on the dependence on $\boldsymbol{x}_0$ and t_0, to simplify the notation.

Furthermore, we define a 2-dimensional time-dependent orthonormal basis, centred on $\boldsymbol{B}(t)$, and whose axes are the line connecting $\boldsymbol{x}_0$ to $\boldsymbol{B}(t)$, and its perpendicular. The components/coordinates of $\boldsymbol{g}_i(t)$ on this basis are hereafter denoted as $b_{i,\parallel}(t)$ and $b_{i,\perp}(t)$, as illustrated in the bottom panel of Fig. 1; they provide informations on the spatial and temporal evolution of the ensemble spread and shape, and can also be used to look at how the virtual buoy positions are distributed around the ensemble mean over time.

With the individual r_i and b_i in hands, we compute basic, second-order, statistics. Let consider their means, μ_r and μ_b,

$$\mu_r(t) = \frac{1}{N} \sum_{i=1}^{N} r_i(t), \qquad \mu_b(t) = \frac{1}{N} \sum_{i=1}^{N} b_i(t), \tag{8}$$
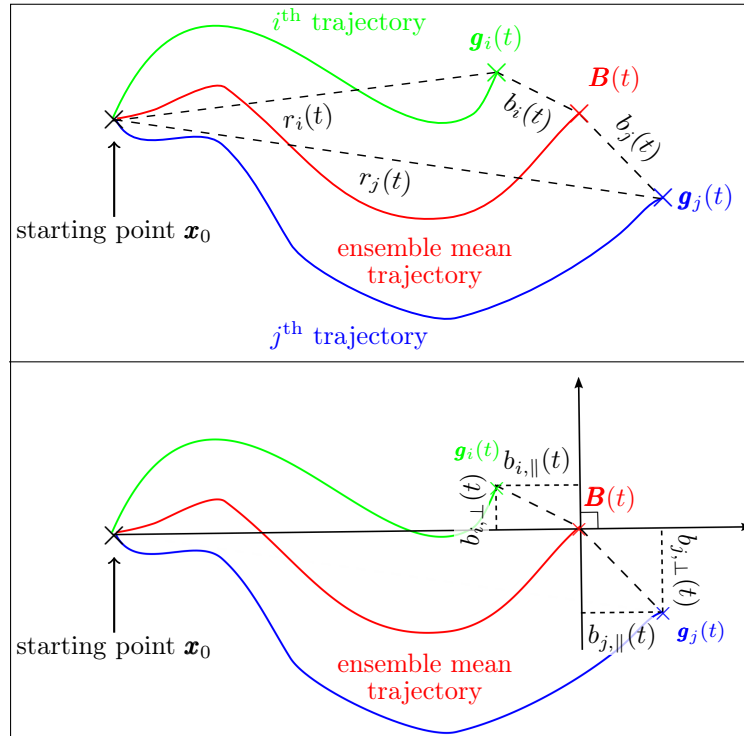
The Cryosphere
Discussions

Open Access

EGU

Figure 1. From a 12 bouquet of simulated trajectories of a virtual buoy drifting during 10 days of which only two of them, denoted i and j, are drawn, we represent the distances r, b (top) and the coordinates $b_\parallel$, $b_\perp$ (bottom) for the virtual buoy i and j at time t.

and the standard deviations, $\sigma_{b_\parallel}$ and $\sigma_{b_\perp}$, of the components $b_\parallel$ and $b_\perp$,

$$\sigma_{b_\parallel}(t) = \sqrt{\frac{1}{N-1}\sum_{i=1}^{N}\left|b_{i,\parallel}(t)\right|^2} \quad \text{and} \quad \sigma_{b_\perp}(t) = \sqrt{\frac{1}{N-1}\sum_{i=1}^{N}\left|b_{i,\perp}(t)\right|^2}, \tag{9}$$

as our main quantities of interest in the analysis that follows. In particular, we use the standard deviations to compute the ratio

$$R(t) = \sigma_{b_\parallel}(t)/\sigma_{b_\perp}(t), \tag{10}$$

5   that provides a measure of the anisotropy of the ensemble spread of the virtual buoys positions around the barycentre B of the ensemble.

It is finally worth observing that the two quantities, r and b, provide complementary informations: the former about the advective component of the motion, whereas the latter on its diffusive part. The ensemble mean distance from the starting

10   point, μ_r is a statistical estimate of the distance travelled by an ice parcel according to the ice advection properties of the motion field, while μ_b is the (mean) spread relative to the aforementioned distance and accounts for the diffusion properties of the motion; see the top panel of Fig. 1.
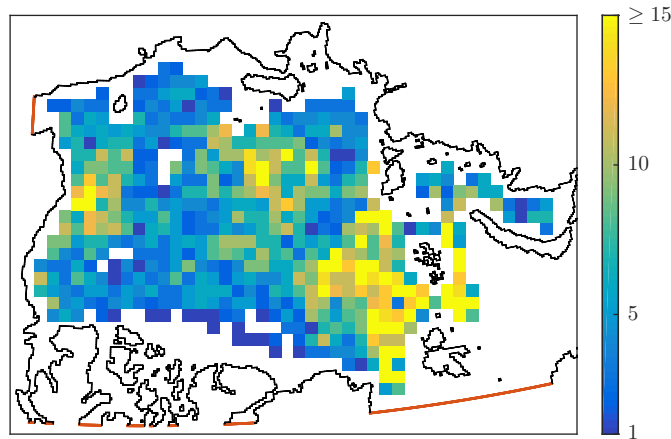
Figure 2. Spatial distribution of the number of occurrences of free drift events between 1 January 2008 and 30 April 2008. These are the instances used for the optimisation of the air drag coefficient.

3.2 Experimental setup

Our domain of study is the region covering the Arctic Ocean. While the coasts are considered as closed boundaries, open boundaries are set at the Fram and Bering Straits (see Fig 4).

5   The wind forcing is taken from the Arctic System Reanalysis (ASR) (Bromwich et al., 2012). This reanalysis product provides wind speeds and direction every 3 hours and at a horizontal resolution of 30 km. For every 3-hourly wind field, we generate spatio-temporal correlated perturbations as described in Evensen (2003), and then add them to the basic wind field from the ASR. This procedure is identical to the one used to produce ensemble runs with the coupled ocean–sea ice model TOPAZ (Sakov et al., 2012; Melsom et al., 2012). The main advantage of the method is that the perturbed wind fields are

10   keeping important physical properties, that is, the wind perturbations are geostrophic (gradients of random perturbations of the sea level pressure) and the wind divergence is kept almost unchanged. They are built on random stationary Gaussian fields, with a Gaussian spatial covariance function, dimensionalised by the wind error variance and correlated in time. Time series of wind perturbations are assumed to be red noise. For our study, we used a decorrelation time-scale of 2 days, a horizontal decorrelation length scale of 250 km, the and the wind speed variance as equal to 1 m^2 s^{-2}. These values are identical to those

15   used in Sakov et al. (2012) except for a reduced wind speed variance (6 times smaller).

Although the ensemble average of the perturbations is equal by construction to the original wind directions provided by the ASR reanalysis, the wind speed is positively biased. The value of the air drag coefficient (C_a in Eq. (7)) had previously been optimised in the *neXtSIM* model when forced by the ASR reanalysis following a method described in Rampal et al. (2016b),

20   Sect. 3.2, and set to 7.6×10^{-3}. We applied the same method here to tune the value of C_a so that the simulated ice drift compare
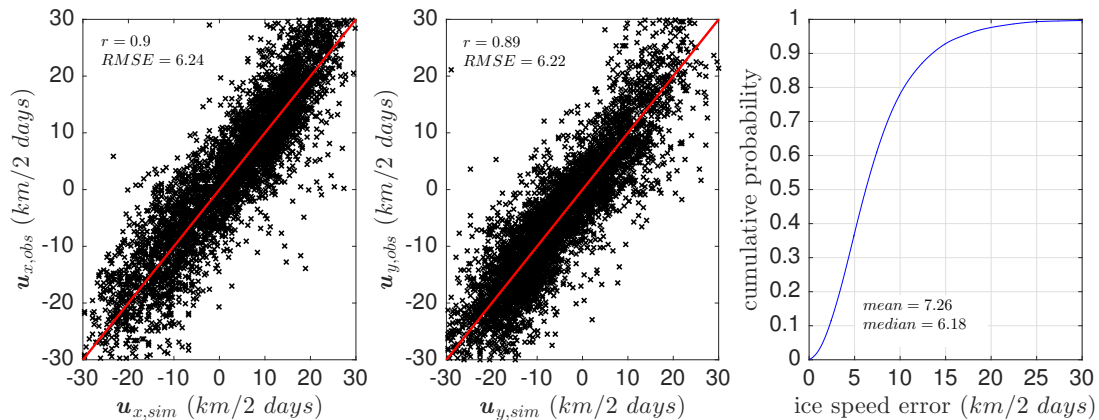
Figure 3. Scatter plots for the two components, x (left) and y (center), of the simulated (*neXtSIM*, x-axis) and observed drift (OSISAF dataset, y-axis) after the air drag optimisation procedure. The cumulative distribution of the ice velocity errors is shown in the rightmost panel.

best with the observed ice drift from the OSISAF dataset (Lavergne and Eastwood, 2015). The optimisation is carried out at all times but limited to the region where the ice is in free-drift (see Fig. 2).

Figure 3 shows the comparison, after optimisation of the air drag coefficient, between the observed and simulated ice veloc-
5 ities. As expected for a wind dataset positively biased in magnitude compared to the original one, we found an optimized value for the drag coefficient $C_a = 5.1 \times 10^{-3}$, lower than the one used in Rampal et al. (2016b) (7.6×10^{-3}).

The ocean forcing comes from the TOPAZ4 reanalysis (Sakov et al., 2012). TOPAZ4 is a coupled ocean-sea ice system combined with a state-of-art ensemble Kalman filter data assimilation scheme assimilating both ocean and sea ice observations. In
10 our simulations, we used the $30\,m$ depth currents, the surface temperature and salinity, and the sea surface height, all provided as daily means with an average horizontal resolution of $12.5\,km$, following Rampal et al. (2016b).

Our analysis is based on two periods of the year 2008, respectively from 1 January to 10 May and from 1 July to 20 September, representative of the winter and summer conditions. We have intentionally studied them separately, because winter and
15 summer are characterised by significantly different sea ice mechanical regimes, and therefore drift responses. During the winter, the whole Arctic basin is covered by ice and its concentration is close or equal to 100%, that is, the internal stresses in the ice, and the corresponding $\nabla \cdot (\boldsymbol{\sigma} h)$ term in Eq. (2), becomes very large and dominant. As a consequence, the ice drift is (on average) much reduced. During the summer period, on the other hand, the ice concentration is lower and the ice pack does not generally reach the coasts, the ice internal stresses are close or equal to zero, and the ice drift closer to a *free-drift* state (see
20 text below). We remark however that the wind field perturbations are generated using the same procedure aforementioned, for
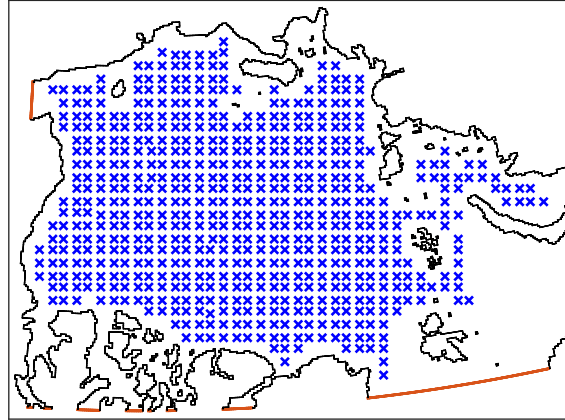
Figure 4. Maps showing the Arctic domain considered for this study. The red lines are open boundaries, while the black coastlines are closed boundaries. The starting points of the ensemble trajectories simulated with the *neXtSIM* and FD models are represented by the blue crosses.

both the winter and the summer, and have thus the same spatial and temporal properties.

We ran a total of 13, in the winter, and 8, in the summer, simulations for successive non-overlapping 10-days long periods. Limiting the length of the simulations to 10 days ensures that the thermodynamical effect (increase in sea ice concentration or thickness) on the drift can reasonably be considered negligible along the track. The starting positions are spaced by 100 km and cover the domain as displayed in Fig. 4. We ran an ensemble of 12 members, each of them forced by the perturbed wind dataset generated as explained above. We performed (not shown) a convergence analysis of our results as a function of the ensemble size from $N = 3$ to $N = 20$, and observed a convergence from about $N = 10$ with only minor changes for $N \geq 12$, and are thus confident that $N = 12$ suffices to our purposes. From these ensemble runs we simulated a total of 8000 virtual buoy trajectories over the winter season, and around 3200 trajectories over the summer season. This dataset was used to run the analyses described in Sect. 4 and presented at the 19th EGU General Assembly (Rabatel et al., 2017).

As already stated, we compared *neXtSIM* with the so-called *free-drift* model, hereafter referred to as FD, so that all simulations that follow have been carried out for the two models. *neXtSIM*, Eq. (2) with all terms in its right-hand-side included, is our reference model. The FD model is equivalent to *neXtSIM* except that it considers the following simplified version of the momentum equation in which the terms related to the sea ice rheology and the inertial term are neglected

$$0 = \boldsymbol{\tau}_\mathrm{a} + \boldsymbol{\tau}_\mathrm{w} - mf\boldsymbol{k} \wedge \boldsymbol{u} - m\boldsymbol{g}\nabla\eta. \tag{11}$$

In Eq. (11) the water and air drag forces, the Coriolis force and the gravity force due to the ocean surface tilt are balancing each other. The FD model therefore mimics the drift of a buoy at the surface of the ocean.

4 Results

In this section, the notations $< . >_W$ and $< . >_S$ correspond to winter and summer averages (i.e. over all the 13 and 8 simulation periods of 10 days) respectively. The notations $< . >_D$ correspond to the spatial mean over the domain. When considering both spatially and temporally averaged quantities, we use the notations $< . >_{W,D}$ or $< . >_{S,D}$.

4.1 Spatial patterns

Figures 5 and 7 show maps of mean drifting distance and spread (see the definitions of μ_b and μ_r in Sect. 3.1) of the virtual buoys after $t = 10$ days, averaged over the 13 (winter) and 8 (summer) successive simulations. Similar results are obtained for different time $t \in [0, 10]$ days (not shown). The pixels on the maps correspond to boxes of $100 \times 100\ km$ centred on the initial positions $\boldsymbol{x}_0$ where the virtual buoys have been deployed at t_0.

Figures 6 and 8 are the counterparts of Figs. 5 and 7 and show the average wind speed (left panel) and ice thickness (right panel) for winter (Fig. 6) and summer (Fig. 8) respectively. Note that both figures are relative to *neXtSIM*, but the free-drift wind speed is identical (same perturbations) and the ice thickness geographical pattern very similar; we have thus omitted to display them to avoid redundancy.

From Fig. 5 and 7 we see that *neXtSIM* gives a smoother response to perturbed forcing than the FD model in terms of mean advective drift μ_r and mean diffusive spread μ_b, in both winter and summer. Indeed, we observe in *neXtSIM* a clear spatial coherency in both the advection and diffusion of the ice buoys over the domain that is almost completely absent in FD for which the obtained fields appear almost random. We believe that this behaviour is related to the mean ice thickness pattern and, to a lesser extent, to the mean wind speed pattern (see Figs. 6 and 8 for winter and summer respectively).

For *neXtSIM*, the smallest values for the mean of μ_r and μ_b averaged over the winter time period are found in the area located north of Greenland and the Canadian Archipelago, which is where the ice is the oldest, thickest ($> 4\ m$) and mechanically the strongest, and where the winds are on average weaker as compared to the rest of the Arctic. On another hand, in the surrounding Seas (i.e. Beaufort, Bering, Chucky, Kara and Barents Seas from West to East), where the ice is thinner and the winds stronger, the mean of μ_r and μ_b are larger. Note that in summer these correlations or anti-correlations are even stronger, for example between the means of μ_b and the ice thickness (see Figs. 7 and 8).

For FD, and for both winter and summer, the mean values of μ_r are less correlated to the thickness field than in *neXtSIM*, but still strongly correlated to the wind speed (left panels inn Fig. 6 and 8), whereas the spatial pattern of the mean of μ_b shows no coherence compared to *neXtSIM* and looks noisy. It is worth noting that, despite the presence of thick ice in the north of the Canadian Archipelago and low winds, the ice is still advected significantly, as opposed to what is obtained with *neXtSIM*.
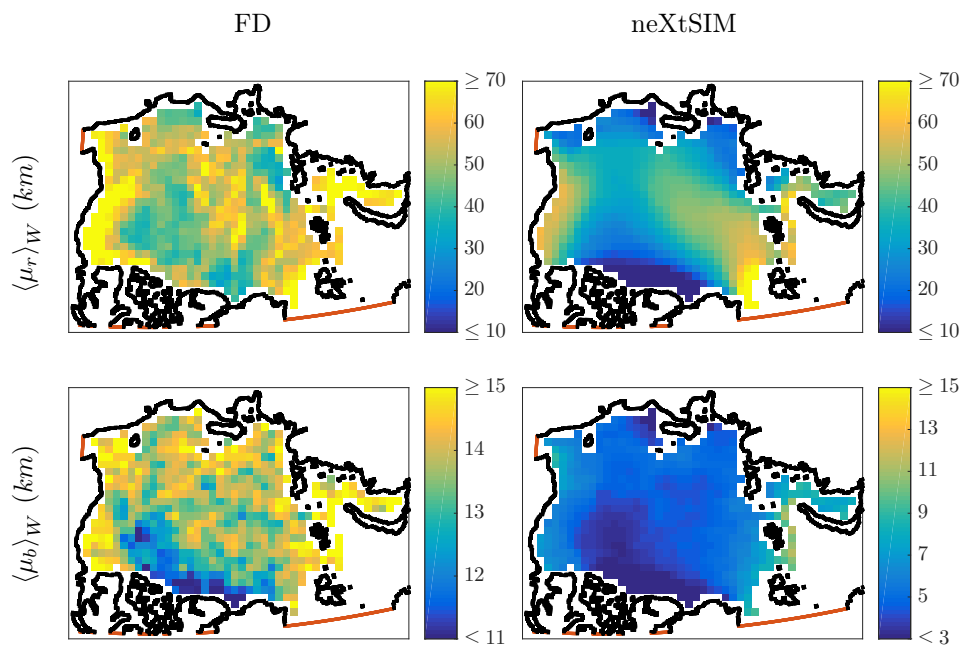
FD   neXtSIM

Figure 5. Mean over the winter period of $\mu_r(t)$ and $\mu_b(t)$ at $t = 10$ days. The calculated values are represented by coloured squares centred on the starting points $\boldsymbol{x}_0$ shown in Fig. 4.

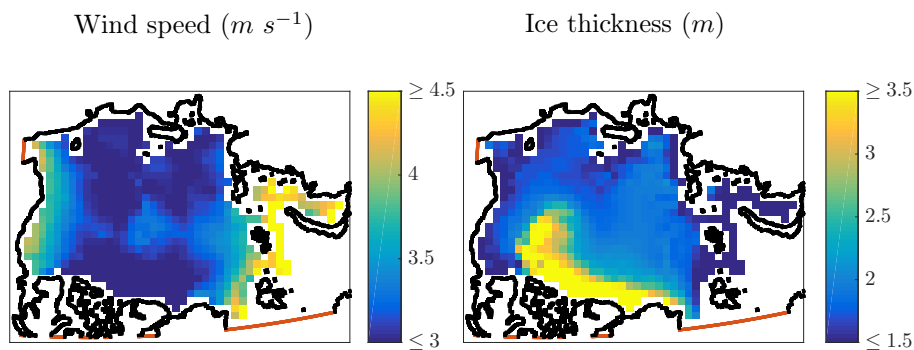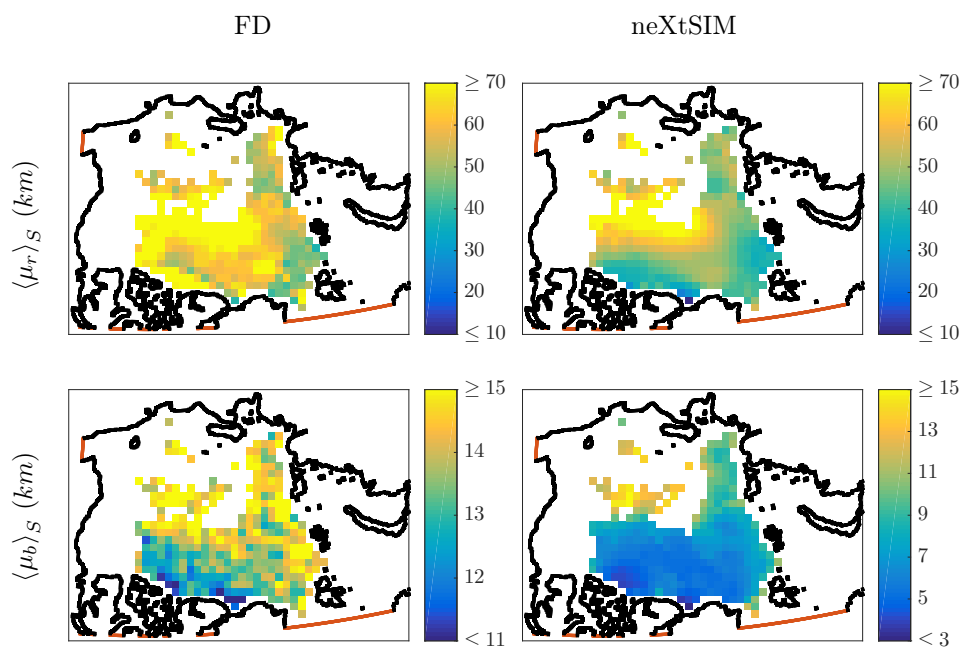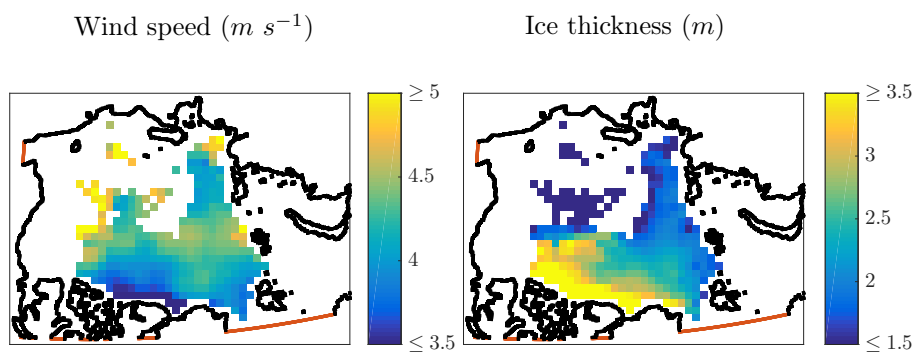Wind speed $(m\ s^{-1})$ Ice thickness (m)

Figure 6. Winter average of wind speed and ice thickness. Both maps are from the *neXtSIM* simulations, but similar thickness field and exact same wind speed field are obtained for the FD simulations.

Figure 7. Mean over the summer period of $\mu_r(t)$ and $\mu_b(t)$ at $t = 10$ days. The calculated values are represented by coloured squares centred on the summer starting points x_0 (not shown).

Figure 8. Summer average of wind speed and ice thickness. Both maps are from the *neXtSIM* simulations, but similar thickness field and exact same wind speed field are obtained for the FD simulations.

In both winter and summer, the response to wind perturbations is overall lower by 35% in *neXtSIM* than in FD. This can be attributed to the fact that the ice rheology is taken into account in *neXtSIM*, thus acting as an additional filter on the momentum transferred from the wind to the ice. In more details, it is interesting to note that the magnitude of the impact of the ice rheology is different whether we look at the drifted distance by advection r or the spread distance by diffusion b and during the winter or the summer. Averaged over the winter, $\langle \mu_r(t) \rangle_D$ and $\langle \mu_b(t) \rangle_D$ are respectively 35% and 63% lower in *neXtSIM* than in FD at $t = 10$ days, whereas over the summer, $\langle \mu_r(t) \rangle_D$ and $\langle \mu_b(t) \rangle_D$ are respectively 14% and 39% lower. This large difference between the two distances, especially in winter, is probably related to the high ice concentration making sea ice harder to break up, and keeps the members closer to each other. During summer, the ice is generally much less packed and the physical/dynamical differences between *neXtSIM* and FD have a lower impact.

As expected, for *neXtSIM*, we observe an increase of $\mu_r(t)$, of about 51%, and $\mu_b(t)$, of about 69%, in summer compared to winter. This behaviour differs drastically from the FD for which the values are nearly the same for both periods, and it is presumably related to the decrease in ice concentration due to the summer melting. The averaged sea ice concentration over the whole domain in winter is about 0.99 while it drops to 0.83 in the summer. In *neXtSIM*, this strongly influence the mechanical behaviour of the sea ice since the effective elastic stiffness E depends non linearly on the ice concentration (see Eq. (5)). Assuming no change in the average level of damage of the ice, a drop by 15% of the ice concentration between winter and summer implies a reduction of E by 96%. This reduction of E leads in turn to a significant decrease of the internal stresses within the ice, thus lowering the term $\nabla \cdot (\boldsymbol{\sigma} h)$ in Eq. (2), which makes the buoy's drift in *neXtSIM* closer to the one obtained with the FD model.

The absolute values of μ_r and μ_b obtained by our analysis reveal that the advection part of the motion is in general larger than the diffusive part, independently of the season under consideration. In FD the ratio $\gamma = \mu_r(t)/\mu_b(t)$ at $t = 10$ days is about 4. In *neXtSIM* though, the ice rheology is acting in increasing this ratio to 7. However, this value presents a strong spatial variability depending on the local thickness and wind speed. Where both are large, γ is large. For example, such areas are observed in the Fram Strait in winter ($\gamma > 10$), and in the central Arctic in summer ($\gamma > 12$). Where both ice thickness and wind speed are small, γ is small. For example, this is the case around the new Siberian islands in winter ($\gamma < 4$), and close to the ice pack edge in summer ($\gamma < 6$).

4.2 Spatial and temporal properties of the ensemble spread

Figure 9 shows the probability density function (PDF) of $b_\parallel(t)$ and $b_\perp(t)$ at $t = 10$ days for both *neXtSIM* and FD, and for winter and summer (see Sect. 3.1). The PDFs of $b_\parallel$ and $b_\perp$ for the FD case are almost identical, thus we chose to only display one curve (black dashed line). The first aspect to remark from Fig. 9 is that all distributions are uni-modal and symmetric, suggesting that the 2D-shape of the ensemble is symmetric around its barycentre $\boldsymbol{B}$. However, we notice that the ensemble is anisotropic in *neXtSIM*, that is, the distributions of $b_\parallel$ and $b_\perp$ differ substantially, whereas it is close to isotropic in FD.
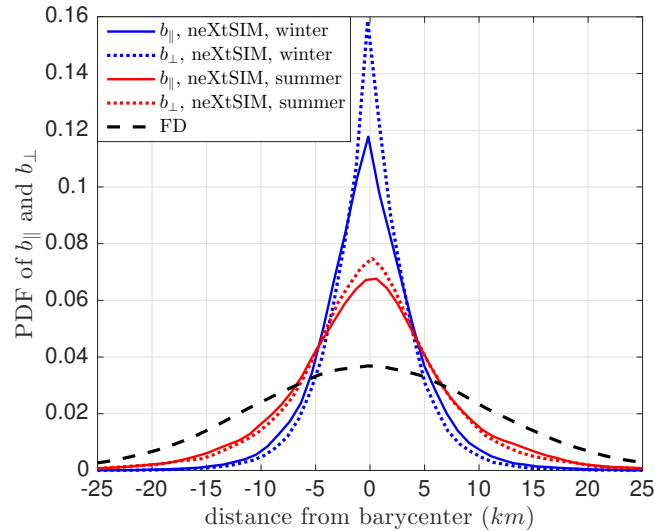
The Cryosphere
Discussions

Figure 9. Probability density function of $b_\parallel(t)$ (solid lines) and $b_\perp(t)$ (dotted lines) at $t = 10$ days for *neXtSIM* in the winter (blue) and summer (red). The PDFs from FD are similar for summer and winter, and for $b_\parallel(t)$ and $b_\perp(t)$, and are therefore shown as a single black dashed line.

Figure 10 shows the temporal evolution over 10 days of the Arctic-averaged ratio R, Eq. (10), that defines the degree of anisotropy of the ensemble spread (1: isotropic; > 1: anisotropic). We observe that R is very close to 1 and relatively constant over time in the FD model. On another hand, it is systematically larger in *neXtSIM*, especially in winter, and it also displays a certain short-term variability. Here again, we encounter the peculiar effect of the *neXtSIM* mechanical response to the external

5   forces, which is to break up and deform along fractures that are dispersing the different members of the ensemble along a preferential direction; such a behaviour cannot be reproduced by the FD. Note also that R is as large as 2 within day 1 and 2 for *neXtSIM* in the winter, and it then monotonically decrease for $t > 2$, but it still remains very large (between 1.4 and 1.6 at $t = 10$ days). This reveals that the ice will first tend to move compactly along the wind direction away from the origin, but it then starts to break and depart from the barycentre.

10

In Fig. 11, we show the maps of the $R(t)$ values computed for each ensemble of trajectories at $t = 10$ days. These values are represented as coloured squares centred on the starting point x_0. We observe that highest degree of ensemble anisotropy ($R > 1$) is found north of Greenland and Canadian Archipelago, where the ice is the thickest and the ice drift and winds the lowest, in overall agreement with the interpretation of the temporal evolution of R for *neXtSIM* in the winter, provided in

15   relation with Fig. 10. Similarly, as already noticed from Fig. 10, the values obtained for *neXtSIM* are systematically larger (of about 65%) than for FD during the winter whereas only 8% larger during the summer. Yet, and remarkably, the values of R,
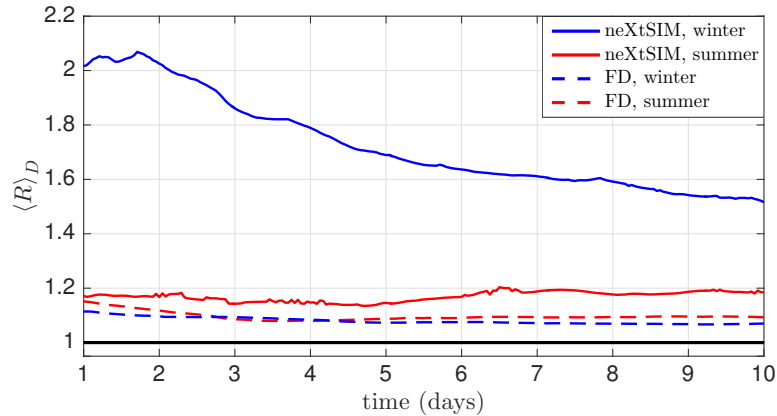
Figure 10. Evolution of the spatial mean of $R(t)$ from $t = 1$ to $t = 10$ days for the winter (blue) and summer (red) periods for *neXtSIM* (solid lines) and FD (dashed lines).

and thus the anisotropy of the ice drift, for *neXtSIM* exhibit marked spatial correlations that are almost absent in FD.

Another important characterisation of the ensemble spread evolution can be set by looking at the variance of the distance b between the virtual buoys and the barycentre $\boldsymbol{B}$ over time. The goal is to identify the diffusion characteristics of the ensemble, which can be interpreted in the framework of the turbulent diffusion theory of Taylor (1921). Similar Lagrangian diffusion analysis has been applied to study the regimes of diffusion of surface drifters in the ocean (e.g. Zhang et al., 2001; Poulain and Niiler, 1989), and more recently of buoys fixed to the ice cover (e.g. Rampal et al., 2009; Lukovich et al., 2015; Gabrielski et al., 2015; Rampal et al., 2016a). In the analysis performed here, the distance b to the barycentre of the ensemble corresponds to the fluctuating part m' of the motion m in the so-called *Taylor's decomposition* $m = \overline{m} + m'$. Figure 12 shows the temporal evolution of the ensemble average of the distances b_i averaged over the Arctic domain D calculated form the buoy's tracks simulated with *neXtSIM* and FD. We found that the ensemble spread follow two distinct diffusion regimes, one for small time $t \ll \Gamma$ and one for large time $t \gg \Gamma$ where Γ is the so-called *integral time scale* (Taylor, 1921), which is about 1.5 days for sea ice according to Rampal et al. (2009). In *neXtSIM*, the first regime we found corresponds to the *ballistic* regime where $\left\langle \langle b_i^2 \rangle \right\rangle_D \sim t^2$, and the second to the *Brownian* regime where $\left\langle \langle b_i^2 \rangle \right\rangle_D \sim t$. These two regimes are reproduced by *neXtSIM* in our winter simulations. These results are in agreement with the sea ice diffusion regimes revealed by applying the Lagrangian diffusion analysis to the buoy trajectories dataset of the International Arctic Buoy Programme (Rigor, 2002) (Rampal et al., 2009), and shows that our experimental setup based on ensemble simulations forced by perturbed winds does not alter the capability of the *neXtSIM* model to reproduce the properties of sea ice diffusion that was reported recently in Rampal et al. (2016a). One should note that for FD, for both periods, and for *neXtSIM* during the summer, $\left\langle \langle b_i^2 \rangle \right\rangle_D \sim t^{1.15}$ for $t \gg \Gamma$ meaning that the simulated growth of the ensemble is *super-diffusive* and in disagreement with the observations.
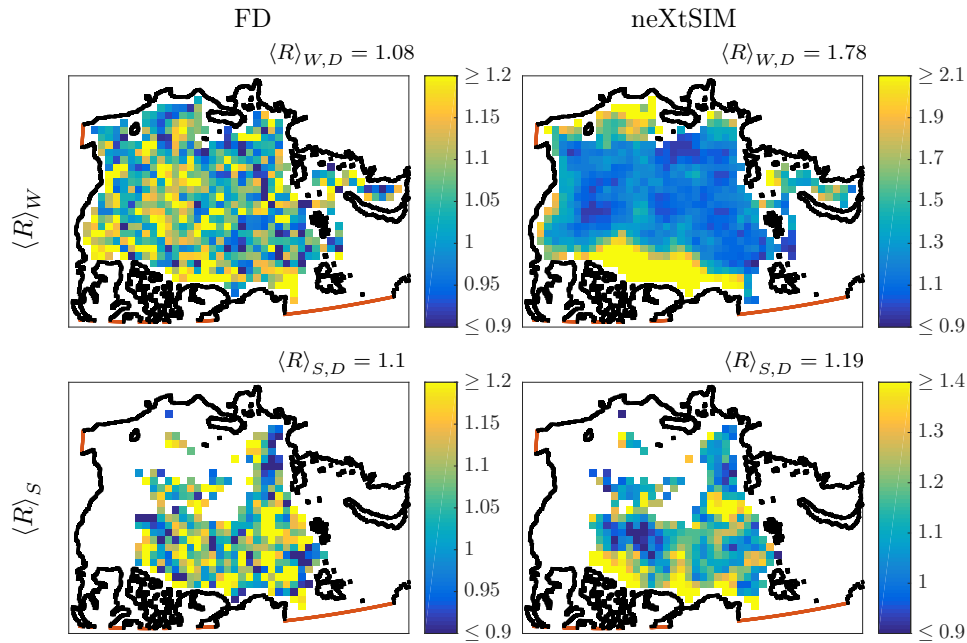
Figure 11. Means over the winter (top panels) and summer (bottom panels) of $R(t)$ at $t = 10$ days. The values are represented by coloured squares centred on the starting points $\boldsymbol{x}_0$. The spatio-temporal mean values (i.e. domain averaged and seasonally averaged) are calculated for each model and displayed above each panels for reference.

4.3 Predictive skills of *neXtSIM* and of the FD models

We evaluate here how well *neXtSIM* and FD models are able to forecast real trajectories. As a benchmark, we compare the ensemble runs from each model to 604 (in winter) and 344 (in summer) observed trajectories from the IABP dataset. The simulated trajectories of both *neXtSIM* and FD are initiated on the same initial positions and at the same time as the IABP

5   buoys, and are displayed in Fig. 13; the positions of IABP buoys are known every 12 hours.

As a metric for the models skill inter-comparison, we use the linear *forecast error* vector

$$\boldsymbol{e}(t) = \boldsymbol{B}(t) - \boldsymbol{O}(t), \tag{12}$$

defined as the distance between the observed IABP buoy position, $\boldsymbol{O}(t)$, and that of the ensemble mean, $\boldsymbol{B}(t)$ (see also Fig.

10   15). The components of $\boldsymbol{e}(t)$ onto the orthonormal basis centred on $\boldsymbol{O}$ (see Sect. 3.1, Fig. 1 and 15), read $e_\parallel(t)$ and $e_\perp(t)$.

Figure 14 shows the average module of the forecast error, $\|\boldsymbol{e}\|$, and of its components, $e_\parallel(t)$ and $e_\perp(t)$, as a function of time, for the experiments with *neXtSIM* and FD, and for both winter and summer. Results reveal that the forecast error is smaller in *neXtSIM* than FD in both seasons. In winter, the error of the FD model grows almost twice as fast as the error of *neXtSIM*, up
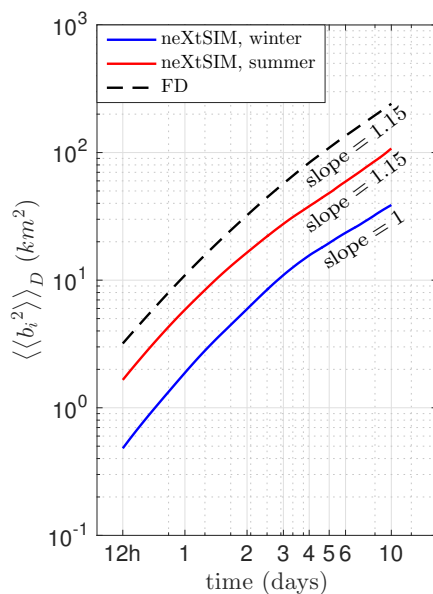
Figure 12. Spatial domain average of the variance of the distances b_i as a function of time from $t = 12$ hours to $t = 10$ days, for the *neXtSIM* (solid) and FD (dashed) models, and for winter (blue) and summer (red). The results for winter and summer being identical in FD, only one curve is plotted (black dashed line). The Brownian regime (slope $= 1$) is reached by *neXtSIM* during the winter, while in the other cases, a *super-diffusive* regime is obtained (slope $= 1.15$).
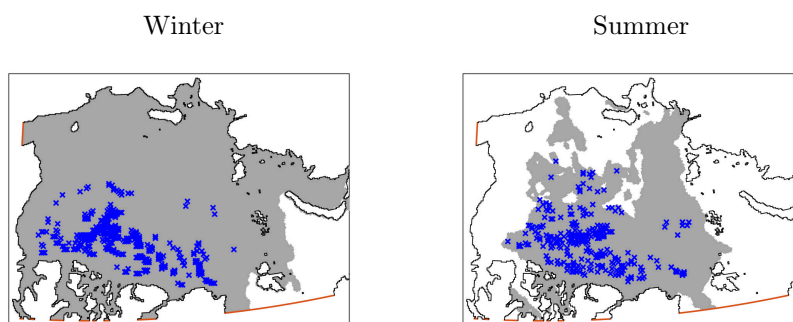

Figure 13. Maps showing the positions (blue crosses, 603 during winter and 344 during summer) of the IABP buoy's trajectories dataset used in this study as starting point of the ensemble trajectory simulations performed with the *neXtSIM* and FD models. The grey area is showing the mean sea ice coverage over the period considered for the simulations.
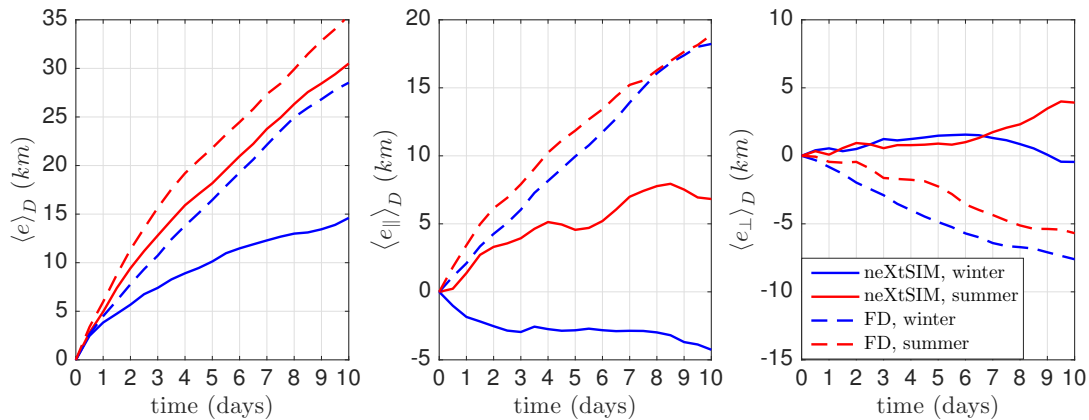
Figure 14. Mean of the absolute forecast error $\|\boldsymbol{e}\|$ and vector components $e_\parallel$ and $e_\perp$ in the directions along and across the mean trajectory, as a function of drift duration. *neXtSIM* is represented by solid lines, while FD is shown as dashed lines. Winter is in blue and summer in red.

to $28.5\ km$ at day 10 compared to $14.6\ km$ for *neXtSIM*.

As already deduced from the results in the previous section, the mechanics underlying of the ice drift in *neXtSIM* and FD get very similar in the summer, and this is reflected by the two errors being much closer to each other: the difference between the two increases slower, reaching $\simeq 4\ km$ after 4 days (see the left panel in Fig. 14). The central panel in Fig. 14 shows a positive bias of the error in the along-drift component ($e_\parallel$) for both models and both periods, except for *neXtSIM* in winter which presents a negative bias. Nevertheless, the biases in *neXtSIM* are all as small as one third of the corresponding ones in the FD model. The general positive biases betray a too fast drift in the direction along the ensemble mean drift compared to the observations. Finally, the right panel in Fig. 14 also reveals a bias of the error in the direction across the ensemble mean drift, yet substantially weaker than in the previous case. For FD, $e_\perp$ still being positive for both periods, corresponds to a drift too far to the right in the observations. This bias should be explained by the fact the Coriolis effect depends on the velocity, which is generally higher in the FD model; the larger the velocity the larger the Coriolis effect. With *neXtSIM*, these biases are much weaker in both periods. Overall, the performances are best for *neXtSIM*, especially in winter.

In Hackett et al. (2006); Breivik and Allen (2008), Monte Carlo techniques are used to forecast the drift of an object on the ocean surface. They associate the density of trajectories at their end points to a density of probability and use them to define a search area, within which the object is likely to be found. The search area is characterised by a surface centred on the ensemble mean and which size increases with the ensemble spread. The same methodology is followed here for forecasting the location of an object on drifting sea ice. In the context of rescue operations, the search area should be large enough to contain the actual position of the object, but not excessively large so as to keep the rescue operations time and resources affordable and efficient. The forecast system should therefore ideally yield a high probability to find the object in the search area, while keeping at the
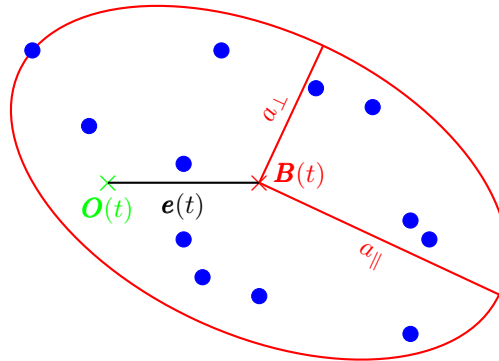
19

The Cryosphere
Discussions

Open Access

EGU

Figure 15. Illustration of the forecast error and the anisotropic search area. Blue dots represents the position of one member, while the barycentre of the ensemble (its mean) is $\boldsymbol{B}(t)$. The observation $\boldsymbol{O}(t)$ is in green and the forecast error is defined in Eq. (12). See text for definitions of the search ellipse and anisotropy ratio.

same time the search area as small as possible for the cost-efficiency of the rescue procedure.

The probability to find the object inside the search area, is referred to as the *probability of containment*, POC, and reads

$$POC \propto \frac{Area}{\|\boldsymbol{e}\|^2}. \tag{13}$$

5   POC is proportional to the ratio of the size of the search area to the square forecast error. A small fore cast error compared to the search area leads to a strong POC; conversely, a small search area (ensemble spread) compared to the forecast error leads to a poor POC.

In order to evaluate the probabilistic forecast capabilities of *neXtSIM* and the more classical FD model, the context of a

10   *search and rescue operation* is adopted. We assume that an IABP buoy has been lost for 10 days: its initial position, $\boldsymbol{x}_0$ (see Fig. 13), is assumed to be its last known position. The search area is then defined as the smallest ellipse centred on the ensemble mean position, $\boldsymbol{B}(t)$, encompassing all simulated ensemble of buoys of at time t. The main axes of the ellipse, $a_\parallel$ and $a_\perp$, are aligned respectively with the parallel and perpendicular directions from the initial position, as defined in Sect. 3.2, and illustrated in Fig. 15. Similarly to Eq. (10) an anisotropy ratio $R = a_\parallel / a_\perp$ can be defined: R can be large due to the sea ice

15   rheology. A search area defined in this way is increasing with the ensemble spread and contains 100% of the ensemble members.

Short of related literature for search and rescue in sea ice, we consider the values of open ocean search areas and POC found in Breivik and Allen (2008) and Melsom et al. (2012), as reference. These are respectively of the order of 1000 km^2 and 0.5, after 2 days of drift in the North Atlantic. We do not expect however a direct correspondence of these values to those

20   of this section. First the sea ice is a solid, held together by the ice rheology, in particular in high concentration areas, so that
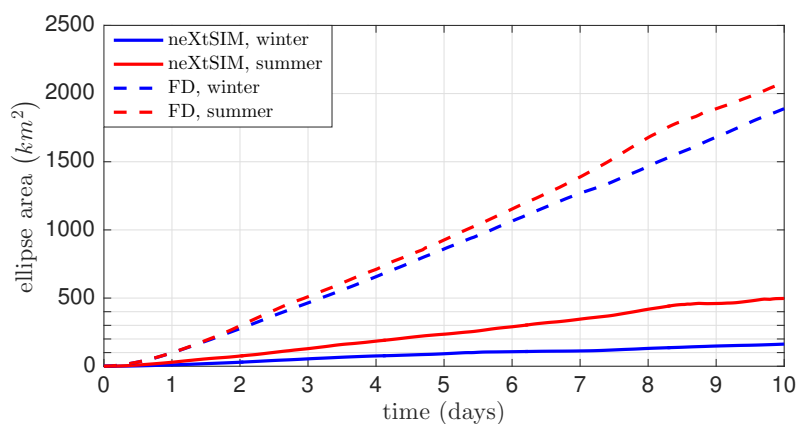
Figure 16. Time evolution of the averaged ellipse areas for *neXtSIM* (solid lines) and FD (dashed lines) in winter (blue) and in summer (red).

the ensemble spread is expected to be smaller than in the open ocean. Second, the currents in the North Atlantic are generally stronger than in the Arctic Ocean. Finally, the search areas may be more complex than just an ellipse; it may well be a set of disjoint areas, each one with an associated different POC (e.g. Abi-Zeid and Frost, 2005; Breivik and Allen, 2008; Guitouni and Masri, 2014; Maio et al., 2016).

Figure 16 shows the evolution of the ellipse areas, averaged over all IABP buoys. The increase is nearly linear for both model configurations and seasons. After 2 days of drift in *neXtSIM*, the area does not exceed $100\ km^2$ in summer and not even half as much in winter. The area is larger in FD, and there is very little difference from winter to summer. The area for the FD is around $300\ km^2$ after 2 days and it almost reach $1000\ km^2$ after 5 days. The search area in FD is about 10 times larger than in *neXtSIM* in the winter and 4 times larger in the summer. Therefore, even if the forecast errors are smaller in *neXtSIM* than in FD, its shrunk search areas lead to a smaller POC for *neXtSIM* than for the FD model (not shown): in practice the probabilistic forecast from *neXtSIM* is *too optimistic*, underestimates the uncertainties in the forecast, while the FD forecast overestimates them.

4.4 Relevance for search and rescue operations

Whether a prediction model is too optimistic or too pessimistic may be equally problematic in view of search and rescue operations. In practice, the resources available for search and rescue operations are limited and only a given area can be covered, although the shape of the area (center and eccentricity in the case of an ellipse) may not influence the cost significantly. Thus, rather than looking at the size of the search area as estimated from the ensemble model prediction, the search-and-rescue operation can posed as follows: for an equal area that can be searched, which model forecast gives the ellipse that is most likely to contain the object?

The ensemble forecast provides the expected position, $\boldsymbol{B}(t)$, and the anisotropy, $R(t)$ of the ellipse as defined previously, but the ellipse area is left free to grow homothetically from $1\ km^2$ to $3000\ km^2$. The POC increases then accordingly as the observed buoy position is more and more likely to fall within the ellipse. The dependency between the search area and the associated POC defines the so called *selectivity curve*, which makes possible a straightforward models comparison: the higher the selectivity curve, the better the model ability to locate the searched object. The selectivity curves allow as also for an immediate evaluation of the rate at which predictive skill is lost as a function of time.

For each time $t_0 + \Delta t$, with $\Delta t \in \{12, 24, 36, 48, \ldots, 10 \times 24\}$ hours, we compute the POC, Eq. (13), corresponding to search areas ranging from $1\ km^2$ to $3000\ km^2$ for both models and seasons. Results from *neXtSIM* (solid lines) and FD (dashed lines) are shown at $t_0 + 1$, 2, 3 and 7 days in Fig. 17. For a given area, the POCs from *neXtSIM* are almost always above those from FD except in two cases: in winter at $t_0 + 1$ day and for search areas larger than $200\ km^2$, and in summer at $t_0 + 1$ day for search areas smaller than $7\ km^2$. As long as the drift is longer than 2 days, the selectivity curves of *neXtSIM* are systematically above FD. For both periods and both models, all curves exhibit a sigmoid shape with an inflexion point, which position depends on the time horizon (higher POC and larger search areas for longer drift duration). For a 7-days drift in winter and a POC equal to 0.5, the area is smaller than $300\ km^2$ with *neXtSIM*, while it reaches $1000\ km^2$ in FD. In the summer, a larger area is necessary to obtain the same POC for both models. For a given search area, the gap between the POCs from *neXtSIM* and FD seems independent from the drift duration in summer, whereas in winter it increases with the time prediction horizon. It is interesting to note the lowermost value of the POC for small areas in winter, which remains above 0.1 for *neXtSIM*. This could be a consequence of the capability of *neXtSIM* to simulate immobile ice, while the FD ice is always in motion with the winds and currents.

How do the different models perform for different forecast time (i.e. drift duration)?

To answer this question, we study the time evolution of the difference between the *neXtSIM* and FD POCs: when this difference is positive/negative *neXtSIM*/FD is outperforming FD/*neXtSIM*. The POC for both models is evaluated for a fixed search area - a vertical section across the selectivity curves - equal to $50\ km^2$ in winter and $175\ km^2$ in summer, and the results are shown in Fig. (18). The chosen values of the search areas, 50 and $175\ km^2$, correspond to the mean ellipse areas based on the ensemble spread from *neXtSIM* after 3 days, averaged over the IABP dataset (see Fig. 16) respectively in winter and in summer. Figure 18 reveals that, after 2 days in the winter, the POC of *neXtSIM* is larger of about 0.2 than the POC of FD; most remarkably, such a substantial improved skill is then maintained almost stably up to the last day of simulation (10 days). During the summer, an the POC of *neXtSIM* is also generally higher than the one of FD, but the difference is half of the one observed in the winter. Furthermore, after the 3$^{\mathrm{rd}}$ day, the difference between the two models decreases up to vanish completely between day 8 and 9. The fact that most of the superiority of *neXtSIM* over reveals during winter is, as stated in previous instances, in full agreement with the expectations, given that during the summer the ice mechanics in the two models is similar.
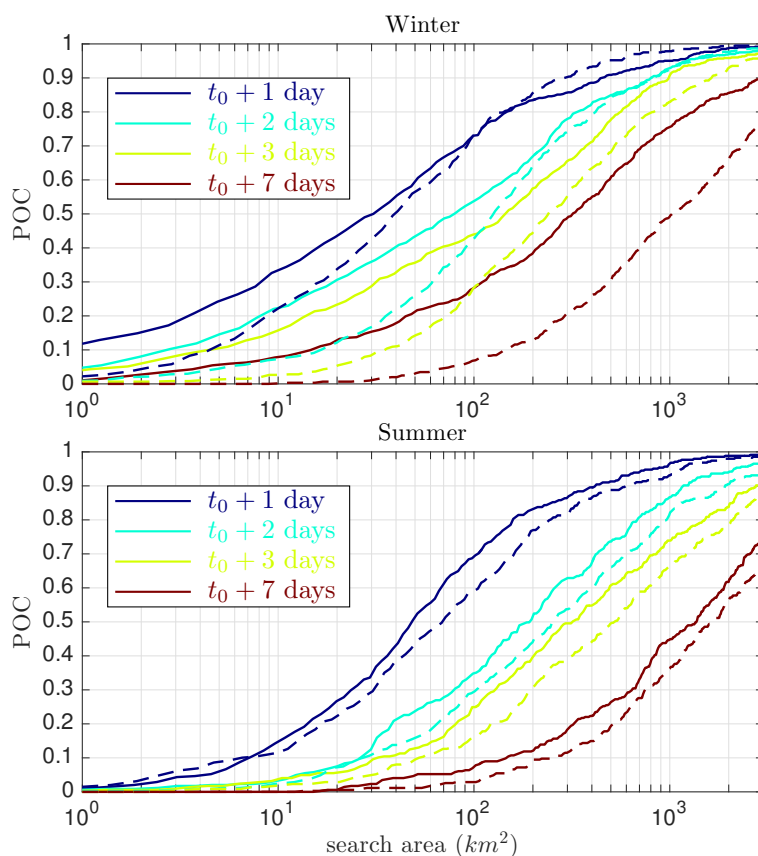
Figure 17. Time evolution of POC according to the search area for *neXtSIM* (solid lines) and FD (dashed lines) in winter (top) and in summer (bottom) for different time horizons.

5 Discussions and Conclusions

The ensemble sensitivity experiment carried out with *neXtSIM* and with a FD model reveals the prominent role of the rheology, which marks the key difference between the two models. On average over the whole Arctic *neXtSIM* is 35% less sensitivity to the wind perturbations than the FD, albeit large seasonal and regional differences are observed. This is exemplified by the

5   imprint of the ice thickness field in the ensemble spread from *neXtSIM* and the much smaller sensitivity of *neXtSIM* in winter than summer, contrarily to the FD model (Fig. 5 and 7). Both aspects point clearly to the role of the rheology which accounts for the ice thickness and compactness. This behaviour should be expected to hold for other sea ice rheologies than the elasto-brittle.

The two models have been tuned on a common dataset of observations of ice in free drift, so that the different performances

10   originate solely by the differences in the resolved model physics. The diffusion regimes of *neXtSIM* and FD are very different
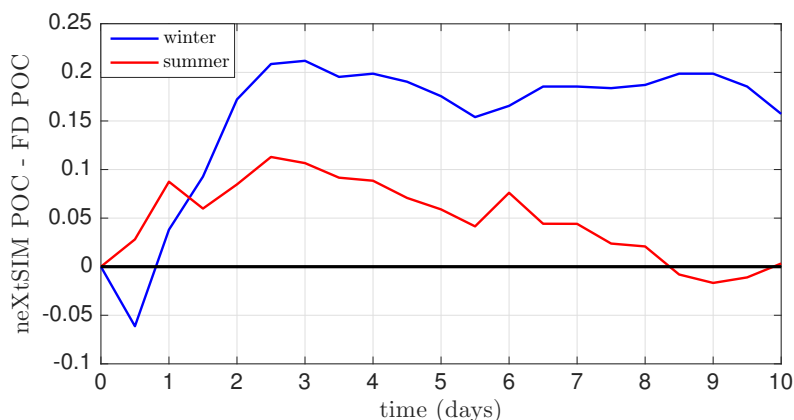
Figure 18. Time evolution of the POC difference between *neXtSIM* and FD for a search area equal to 50 km^2 in winter (blue) and equal to 175 km^2 in summer (red).

(Fig. 12): the offset between the curves indicating differences of sensitivity, and the slopes indicating different rates of increase and thus sea ice diffusivity. The expected differences between summer and winter are only represented when the rheology is turned on.

5   Due to the dispersive properties of the sea ice, the shape of the ensemble of simulated buoys positions is generally anisotropic. Such anisotropy is a signature of the underlying mechanism that drives the dispersion of the members, which is the shear deformation of the ice cover along active faults/fractures in the ice. This mechanism is missing in the absence of rheology (like in the FD model) and represents a clear strength and advantage of the elasto-brittle rheology in *neXtSIM*.

10   The performance of the two models differs significantly when forecasting the trajectories of IABP buoys. The ensemble mean position errors are larger in the summer (5 km after 1 day and 12.5 km after 3 days drift for *neXtSIM*, about 20% below the FD results), and consistent with the values reported by Schweiger and Zhang (2015) (RMS errors of 6.3 km and 14 km respectively, but using different time periods). The corresponding errors are smaller in winter, especially for *neXtSIM* (31% smaller than FD) and down to 4 km for a 1-day drift and 7.5 km for a 3-days drift. These values seem competitive compared 15   to the year-round average RMS error of 5.1 km per day in the TOPAZ4 reanalysis (Xie et al., 2017), even though the ice drift measurements are assimilated in TOPAZ4 (Sakov et al., 2012).

The model sensitivity to winds has been evaluated, yielding (for 10-days drift) a spread from 5 to 10 km, for winter and summer respectively, but this is smaller than the corresponding errors (15 km from the barycentre to the observations in Fig. 20   14). Still, since the diffusion regime is respected (at least in the winter), we are confident that the spread simulated by the model is physically consistent. Alternative sources of biases must be called such as, for example, other model inputs (thickness, con-

centrations, damage, ocean currents). Since the errors are increasing faster in the first days of the simulations, the more likely source of local and short-term errors lies in the position and orientation of the sea ice fracture network, which is not constrained at all in these experiments.

5   Although we would expect an increase of the ensemble spread if the ice thickness, concentrations and ocean currents had been taken into account in the ensemble initialization, yet we do not believe it would lead to a much larger spread, especially in the winter. Still it is the wind forcing being the key player in the spread evolution. We suggest instead that, in the perspective of efficient sea ice forecasting, major efforts should be directed toward assimilating the observed fractures (as of satellite images). The assimilation of fracture (as objects rather than quantitative observations) represents a priori a challenging avenue in

10   terms of data assimilation, which traditionally deals with quantitative scalar or vector observations, however we envision that the damage variable in *neXtSIM*, showing localized features, can be constrained quantitatively to deformation rates as derived from observed high-resolution ice motions and serve as "object assimilation".

In spite of the biases, the selectivity curves indicate that a probabilistic forecast using *neXtSIM* is largely more skilful than

15   the traditional free drift model, and it has the larger potential for practical use in search and rescue operations on sea ice. Since the Arctic is not easily accessible, forecast horizons of 5 to 10 days are probably the most relevant for logistical reasons. On those time scale, the differences of POC shown in Fig. 18 indicate that the free drift model gives a poorer information in winter because of the biases in the central forecast location and the lack of anisotropy, while in the summer the use of a elasto-brittle rheology is only marginally advantageous.

20

The physical consistency of the ensemble sensitivities is a necessary condition to the success of ensemble-based data assimilation methods (Evensen, 2009), which constitutes one of the follow-up research direction the authors are currently considering. Combining the modelling and physical novelty of *neXtSIM* with modern observations of the Arctic is seen as a major asset for forecast and reanalysis applications.

25

Besides the potential use of observations of fractures, as mentioned above, which is indeed another unique advantage of models such as *neXtSIM*, ice drift data are also crucial. Observations of ice drift are still seldom used for data assimilation, and when it is the case, the success is limited by the lack of sensitivity of most the sea ice models (see, e.g. Sakov et al., 2012). Nevertheless, the main fundamental issue related to the use of data assimilation, and particularly ensemble-based, methods,

30   stands in the nature of the Lagrangian mesh of *neXtSIM*, which also include the possibility of re-meshing (Rampal et al., 2016b). This feature, while essential to the skill of the model in describing the mechanics of the sea ice with great details, represents a challenge in developing compatible data assimilation schemes, as the dimension of the state space can change over time when these re-meshing occur. This problem has recently attracted attention in the data assimilation research community (see, e.g. Bonan et al., 2016; Guider et al., 2017) and it is also a main area of on-going investigation of the authors, following

35   the present study.

Author contributions. The sensitivity analysis has been implemented and performed by MR. The results have been analysed by MR, PR, AC and LB. The manuscript has been written by MR and PR, then reviewed and improved with inputs from all authors.

Competing interests. The authors declare that they have no conflict of interest.

References

Abi-Zeid, I. and Frost, J. R.: SARPlan: A decision support system for Canadian Search and Rescue Operations, European Journal of Operational Research, 162, 630–653, 2005.

Bonan, B., Nichols, N. K., Baines, M. J., and Partridge, D.: Data assimilation for moving mesh methods with an application to ice sheet modelling, Nonlinear Processes in Geophysics Discussions, 2016, 1–27, 2016.

Bouillon, S. and Rampal, P.: Presentation of the dynamical core of neXtSIM, a new sea ice model, Ocean Modelling, 91, 23–37, 2015a.

Bouillon, S. and Rampal, P.: On producing sea ice deformation data sets from SAR-derived sea ice motion, The Cryosphere, 9, 663–673, 2015b.

Bouillon, S., Maqueda, M., Legat, V., and Fichefet, T.: An elastic–viscous–plastic sea ice model formulated on Arakawa B and C grids, Ocean Modelling, 27, 174–184, 2009.

Breivik, Ø. and Allen, A. A.: An operational search and rescue model for the Norwegian Sea and the North Sea, Journal of Marine Systems, 69, 99–113, 2008.

Bromwich, D., Bai, L., Hines, K., hung Wang, S., Liu, Z., Lin, H.-C., hwa Kuo, Y., and Barlage, M.: Arctic System Reanalysis (ASR) Project, https://doi.org/10.5065/D6K072B5, 2012.

Buizza, R., Houtekamer, P. L., Pellerin, G., Toth, Z., Zhu, Y., and Wei, M.: A comparison of the ECMWF, MSC, and NCEP global ensemble prediction systems, Monthly Weather Review, 133, 1076–1097, 2005.

Carrassi, A., Guemas, V., Doblas-Reyes, F., Volpi, D., and Asif, M.: Sources of skill in near-term climate prediction: generating initial conditions, Climate Dynamics, 47, 3693–3712, 2016.

Coon, M., Maykut, G., Pritchard, R., Rothrock, D., and Thorndike, A.: Modeling the pack ice as an elastic-plastic material, AIDJEX Bull, 24, 1–105, 1974.

Dansereau, V.: A Maxwell-Elasto-Brittle model for the drift and deformation of sea ice, Ph.D. thesis, Laboratoire de Glaciologie et Géophysique de l'Environnement Grenoble, 2016.

Dobney, A., Klinkenberg, H., Souren, F., and Van Born, W.: Uncertainty calculations for amount of chemical substance measurements performed by means of isotope dilution mass spectrometry as part of the PERM project, Analytica chimica acta, 420, 89–94, 2000.

Duraisamy, K. and Iaccarino, G.: Assessing turbulence sensitivity using stochastic Monte Carlo analysis, arXiv preprint, 2017.

Evensen, G.: The ensemble Kalman filter: Theoretical formulation and practical implementation, Ocean dynamics, 53, 343–367, 2003.

Evensen, G.: Data Assimilation: The Ensemble Kalman Filter, Springer-Verlag/Berlin/Heildelberg, second edn., 2009.

Gabrielski, A., Badin, G., and Kaleschke, L.: Anomalous dispersion of sea ice in the Fram Strait region, Journal of Geophysical Research: Oceans, 120, 1809–1824, 2015.

Girard, L., Weiss, J., Molines, J., Barnier, B., and Bouillon, S.: Evaluation of high-resolution sea ice models on the basis of statistical and scaling properties of Arctic sea ice drift and deformation, Journal of Geophysical Research: Oceans, 114, 2009.

Grumbine, R. W.: Virtual Floe Ice Drift Forecast Model Intercomparison*, Weather Forecast., 13, 886–890, doi:10.1175/1520-0434(1998)013<0886:VFIDFM>2.0.CO;2, 1998.

Grumbine, R. W.: Long Range Sea Ice Drift Model Verification, Tech. Rep. 3, National Centers for Environmental Prediction, Camp Springs, Maryland, 2003.

Guider, C. T., Rabatel, M., Carrassi, A., and Jones, C. K.: Data Assimilation Methods on a Non-conservative Adaptive Mesh, in: EGU General Assembly Conference Abstracts, vol. 19, p. 706, 2017.

Guitouni, A. and Masri, H.: An orienteering model for the search and rescue problem, Computational Management Science, 11, 459–473, 2014.

Hackett, B., Breivik, Ø., and Wettre, C.: Forecasting the drift of objects and substances in the ocean, pp. 507–523, Springer, 2006.

Hebert, D. A., Allard, R. A., Metzger, E. J., Posey, P. G., Preller, R. H., Wallcraft, A. J., Phelps, M. W., and Smedstad, O. M.: Short-term sea
5   ice forecasting: An assessment of ice concentration and ice drift forecasts using the U.S. Navy's Arctic Cap Nowcast/Forecast System, J. Geophy. Res., 120, 8327–8345, doi:10.1002/ 2015JC011283., http://onlinelibrary.wiley.com/doi/10.1002/2015JC011283/abstract, 2015.

Herman, A.: Molecular-dynamics simulation of clustering processes in sea-ice floes, Physical Review E., 84, 2011.

Hibler III, W. D.: A dynamic thermodynamic sea ice model, Journal of Physical Oceanography, 9, 815–846, 1979.

Hopkins, M. A., Frankenstein, S., and Thorndike, A. S.: Formation of an aggregate scale in Arctic sea ice, Journal of Geophysical Research:
10   Oceans, 109, 2004.

Hunke, E. C. and Dukowicz, J. K.: An elastic–viscous–plastic model for sea ice dynamics, Journal of Physical Oceanography, 27, 1849–1867, 1997.

Kwok, R.: Near zero replenishment of the Arctic multiyear sea ice cover at the end of 2005 summer, Geophysical Research Letters, 34, 2007.

Lavergne, T. and Eastwood, S.: Low resolution sea ice drift Product User's Manual - v1.7., Tech. rep., SAF/OSI/CDOP/met.no/TEC/MA/128,
15   EUMETSAT OSI SAF - Ocean and Sea Ice Satellite Application Facility, www.osi-saf.org, 2015.

Leith, C. E.: Theoretical skill of Monte Carlo forecasts, Monthly Weather Review, 102, 409–418, 1974.

Lemieux, J.-F., Tremblay, B. L., Dupont, F., Plante, M., Smith, G. C., and Dumont, D.: A basal stress parameterization for modeling landfast ice, Journal of Geophysical Research: Oceans, 120, 3157–3173, 2015.

Lemieux, J. F., Beaudoin, C., Dupont, F., Roy, F., Smith, G. C., Shlyaeva, A., Buehner, M., Caya, A., Chen, J., Carrieres, T., Pogson, L.,
20   Derepentigny, P., Plante, A., Pestieau, P., Pellerin, P., Ritchie, H., Garric, G., and Ferry, N.: The Regional Ice Prediction System (RIPS): Verification of forecast sea ice concentration, Q. J. R. Meteorol. Soc., 142, 632–643, doi:10.1002/qj.2526, 2016.

Leppäranta, M.: The drift of sea ice, Springer Science & Business Media, second edition edn., 2011.

Leutbecher, M. and Palmer, T. N.: Ensemble forecasting, Journal of Computational Physics, 227, 3515–3539, 2008.

Lukovich, J. V., Hutchings, J. K., and Barber, D. G.: On sea-ice dynamical regimes in the Arctic Ocean, Annals of Glaciology, 56, 323–331,
25   2015.

Maio, A. D., Martin, M. V., and Sorgente, R.: Evaluation of the search and rescue LEEWAY model in the Tyrrhenian Sea: a new point of view, Natural Hazards and Earth System Sciences, 16, 1979–1997, 2016.

Marsan, D., Stern, H., Lindsay, R., and Weiss, J.: Scale Dependence and Localization of the Deformation of Arctic Sea Ice, Physical Review Letters, 93, 178 501, 2004.

30 Melsom, A., Counillon, F., LaCasce, J. H., and Bertino, L.: Forecasting search areas using ensemble ocean circulation modeling, Ocean Dynamics, 62, 1245–1257, 2012.

Molteni, F., Buizza, R., Palmer, T. N., and Petroliagis, T.: The ECMWF ensemble prediction system: Methodology and validation, Quarterly journal of the royal meteorological society, 122, 73–119, 1996.

Motra, H. B., Hildebrand, J., and Wuttke, F.: The Monte Carlo Method for evaluating measurement uncertainty: Application for determining
35   the properties of materials, Probabilistic Engineering Mechanics, 45, 220–228, 2016.

Poulain, P. M. and Niiler, P. P.: Statistical-Analysis of the Surface Circulation in the California Current System Using Satellite-Tracked Drifters, Journal of Physical Oceanography, 19, 1588–1603, 1989.

Rabatel, M., Labbé, S., and Weiss, J.: Dynamics of an assembly of rigid ice floes, Journal of Geophysical Research: Oceans, 120, 5887–5909, 2015.

Rabatel, M., Rampal, P., Bertino, L., Carrassi, A., and Jones, C. K.: Sensitivity Analysis of a Lagrangian Sea Ice Model, in: EGU General Assembly Conference Abstracts, vol. 19, p. 688, 2017.

5 Rampal, P., Weiss, J., Marsan, D., Lindsay, R., and Stern, H.: Scaling properties of sea ice deformation from buoy dispersion analysis, Journal of Geophysical Research, 113, C03 002, 2008.

Rampal, P., Weiss, J., Marsan, D., and Bourgoin, M.: Arctic sea ice velocity field: general circulation and turbulent-like fluctuations, J. Geophys. Res., 114, 2009.

Rampal, P., Weiss, J., Dubois, C., and Campin, J. M.: IPCC climate models de not capture Arctic sea ice drift acceleration: Consequences in
10   terms of projected sea ice thinning and decline, J. Geophys. Res., 116, 2011.

Rampal, P., Bouillon, S., Bergh, J., and Ólason, E.: Arctic sea-ice diffusion from observed and simulated Lagrangian trajectories, The Cryosphere, 10, 1513–1527, 2016a.

Rampal, P., Bouillon, S., Ólason, E., and Morlighem, M.: neXtSIM: A new Lagrangian sea ice model, The Cryosphere, 10, 1055–1073, 2016b.

15 Rigor, I.: IABP Drifting Buoy Pressure, Temperature, Position, and Interpolated Ice Velocity, Version 1. Subset C. Compiled by Polar Science Center. Boulder, Colorado USA. NSIDC: National Snow and Ice Data Center., doi:10.7265/N53X84K7, 2002.

Sakov, P., Counillon, F., Bertino, L., Lisaeter, K. A., Oke, P. R., and Korablev, A.: TOPAZ4: an ocean-sea ice data assimilation system for the North Atlantic and Arctic, Ocean Sci., 8, 633–656, 2012.

Schweiger, A. J. and Zhang, J.: Accuracy of short-term sea ice drift forecasts using a coupled ice-ocean model, Journal of Geophysical
20   Research: Oceans, 120, 7827–7841, doi:10.1002/2015JC011273, http://dx.doi.org/10.1002/2015JC011273, 2015.

Semtner, A. J.: A Model for the Thermodynamic Growth of Sea Ice in Numerical Investigations of Climate, Journal of Physical Oceanography, 6, 379–389, 1976.

Smith, G. C., Roy, F., Reszka, M., Surcel Colan, D., He, Z., Deacu, D., Belanger, J.-M., Skachko, S., Liu, Y., Dupont, F., Lemieux, J.-F., Beaudoin, C., Tranchant, B., Drévillon, M., Garric, G., Testut, C.-E., Lellouche, J.-M., Pellerin, P., Ritchie, H., Lu, Y., Davidson,
25   F., Buehner, M., Caya, A., and Lajoie, M.: Sea ice Forecast Verification in the Canadian Global Ice Ocean Prediction System, Q. J. R. Meteorol. Soc., pp. n/a–n/a, doi:10.1002/qj.2555, http://doi.wiley.com/10.1002/qj.2555, 2015.

Stroeve, J., Holland, M. M., Meier, W., Scambos, T., and Serreze, M. C.: Arctic sea ice decline: Faster than forecast, Geophys. Res. Lett., 34, 2007.

Stroeve, J. C., Serreze, M. C., Holland, M. M., Kay, J. E., Malanik, J., and Barrett, A. P.: The Arctic's rapidly shrinking sea ice cover: a
30   research synthesis, Clim. Change, 110, 1005–1027, 2012.

Taylor, G. I.: Diffusion by continuous movements, Proceedings of the London Mathematical Society, 20, 196–211, 1921.

Thorndike, A. S. and Colony, R.: Sea ice motion in response to geostrophic winds, Journal of Geophysical Research: Oceans, 87, 5845–5852, 1982.

Weiss, J. and Schulson, E. M.: Coulombic faulting from the grain scale to the geophysical scale: lessons from ice, Journal of Physics D:
35   Applied Physics, 42, 214 017, 2009.

Weiss, J., Schulson, E. M., and Stern, H. L.: Sea ice rheology from in-situ, satellite and laboratory observations: Fracture and friction, Earth and Planetary Science Letters, 255, 1–8, 2007.

Wilchinsky, A. V., Feltham, D. L., and Hopkins, M. A.: Effect of shear rupture on aggregate scale formation in sea ice, Journal of Geophysical Research: Oceans, 115, 2010.

Williams, K. D., Harris, C. M., Bodas-Salcedo, A., Camp, J., Comer, R. E., Copsey, D., Fereday, D., Graham, T., Hill, R., Hinton, T., Hyder, P., Ineson, S., Masato, G., Milton, S. F., Roberts, M. J., Rowell, D. P., Sanchez, C., Shelly, A., Sinha, B., Walters, D. N., West, A.,
5   Woollings, T., and Xavier, P. K.: The Met Office Global Coupled model 2.0 (GC2) configuration, Geoscientific Model Development, 8, 1509–1524, doi:10.5194/gmd-8-1509-2015, http://www.geosci-model-dev.net/8/1509/2015/, 2015.

Xie, J., Bertino, L., Counillon, F., Lisæter, K. A., and Sakov, P.: Quality assessment of the TOPAZ4 reanalysis in the Arctic over the period 1991-2013, Ocean Science, 13, 123, 2017.

Zhang, H., Prater, M. D., and Rossby, T.: Isopycnal Lagrangian statistics from the North Atlantic Current RAFOS float observations, Journal
10   of Geophysical Research: Oceans, 106, 13 817–13 836, 2001.

Zhu, Y.: Ensemble forecast: A new approach to uncertainty and predictability, Advances in atmospheric sciences, 22, 781–788, 2005.